INELASTIC CHARGE-TRANSFER DYNAMICS IN DONOR–BRIDGE–ACCEPTOR SYSTEMS USING OPTIMAL MODES

XUNMO YANG[1], ANDREY PEREVERZEV[2], and ERIC R BITTNER[1]

[1]*Department of Chemistry, University of Houston, Houston, TX 77004, USA*
[2]*Department of Chemistry, University of Missouri-Columbia, Columbia, MO 65211, USA*

CONTENTS

I. INTRODUCTION

Photoinitiated electronic energy transport and charge transfer play a central role in a wide range of important chemical and biological processes. They are the fundamental mechanisms for transporting the energy of an absorbed photon to a reaction center in light-harvesting systems and for initiating a wide range of photoinduced chemical processes, including vision, DNA

Advances in Chemical Physics, Volume 163, First Edition. Edited by K. Birgitta Whaley.

mutation, and pigmentation. In general, the rate constant for a chemical reaction expected to be in the Arrhenius form

$$k \propto e^{-E_A/k_B T}, \tag{1}$$

with E_A as the activation energy for the reaction. Central to the theory of condensed phase electron transfer is that the electronic transition from the donor state (D) to the acceptor state (A) occurs on a timescale that is fast compared to the nuclear motion. That is to say that the electron-transfer (ET) reaction is initiated by the electronic transition at the donor geometry followed by a nuclear wave packet motion on the acceptor potential energy surface. This motion can be detected in various ultrafast spectroscopies and has been observed in a number of organic and inorganic systems. Examples include zinc porphyrins [1, 2], heme complexes [2–4], and other metalloproteins [5]. Vibrational coherence has been observed in the accompanying solvent response in the nonadiabatic relaxation of the solvated electron [6]. In fact, in the case of the solvated electron, electronic coherence is dissipated by the ballistic motion of the surrounding water molecules [7–10].

Vibrational coherence has been less commonly observed in simple coordination complexes; one of the most compelling recent examples comes from optical studies of $[Fe(bpy)_3]^{2+}$ reported by Chergui and coworkers [11]. McCusker reports a 164 cm^{-1} damped oscillation in the transient kinetics following electronic excitation corresponding to Cr–O stretching modes that define the "reaction coordinate" for intersystem crossing in $Cr(acac)_3$ [12]. Also, coherent vibrational motion appears to play an important role in the charge-transfer dynamics in both artificial light-harvesting systems [13] and organic polymer heterojunctions [14–17]. Lastly, Weinstein *et al.* recently demonstrated that one can control the branching ratio of an ET reaction by "pushing" specific nuclear motions by an IR pulse following photoexcitation of donor–bridge–acceptor complexes containing a coordinated central Pt atom [18, 19].

The seminal model for calculating nonadiabatic ET rates was developed by Marcus in the 1950s [20–22] and can be summarized in terms of the sketch of the donor and acceptor potential energy curves as presented in Fig. 1. Here, Q is a dimensionless coordinate representing collective nuclear motion. For both the donor and acceptor states, we assume that the electronic energy can be expanded about the respective equilibrium geometries, and V_D and V_A are diabatic potentials for the donor and acceptor states, taking the nuclear configuration of the donor as the energy origin. The thermodynamic driving force ΔG° is given by the free energy difference between the donor and acceptor minima. The activation energy

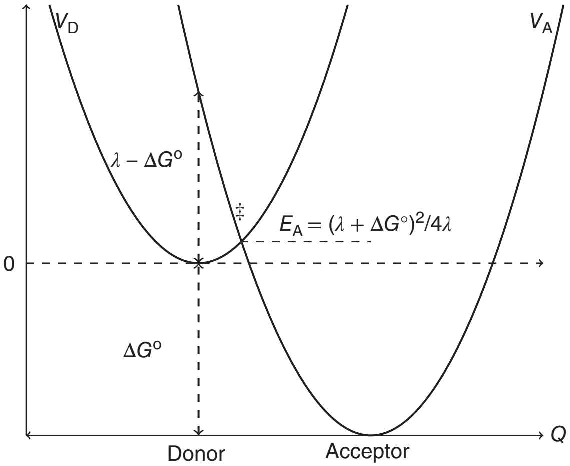

Figure 1. Sketch of Marcus parabolas for a model energy or charge-transfer system. Labeled are the key parameters used to compute the Marcus rate constant (Eq. (3)).

is given by the crossing point between V_D and V_A.

$$E_A = (\lambda + \Delta G^\circ)^2/4\lambda$$

where λ is the energy required to reorganize the environment following the transfer of charge from the donor to the acceptor. In terms of Fig. 1, λ is the change in the electronic energy of the final electronic state when it is brought to the nuclear configuration of the initial state. Since we assume that the potentials are parabolic and identical, λ is also the electronic energy of the initial state in the nuclear configuration of the final state.

Generally, $\lambda - \Delta G^o > 0$ as depicted in Fig. 1, giving an energy barrier E_A at the transition state (denoted as ‡). In the adiabatic regime in which the coupling between electronic terms is comparable to the reorganization energy, the transition occurs on just the lower electronic state. However, if the electronic coupling is small, then the donor and acceptor states retain their "identity" throughout. In this case, Landau–Zener theory can be used to compute the probability for the interconversion of a donor and acceptor via a single passage of the system through the point of intersection of the donor and acceptor diabatic potential curves.

$$P_{DA} = 1 - \exp\left[-\frac{4\pi^2|V_{DA}|^2}{hv|s_D - s_A|}\right] \tag{2}$$

where s_D and s_A are the slopes of the donor and acceptor potentials at the point of intersection, v is the velocity of the system through the intersection region, and V_{DA} is the diabatic coupling. One then arrives at the Marcus equation

$$k_{\mathrm{Marcus}} = \frac{2\pi}{\hbar}|V_{\mathrm{DA}}|^2 \frac{1}{\sqrt{4\pi k_{\mathrm{B}} T\lambda}} e^{-(\lambda+\Delta G^{\circ})^2/4\lambda k_{\mathrm{B}} T}. \tag{3}$$

One of the most profound predictions of the theory is that as the driving force increases, the transfer rate reaches a maximum. This "barrier-less" regime occurs when $\lambda = \Delta G^o$. As the driving force increases, the rates are predicted to decrease. For freely diffusing donor and acceptor species, this inverted behavior proved to be elusive for systems with large driving forces, since in the diffusion limit every encounter between donor and acceptor leads to electron transfer [23]. The existence of the inverted region was demonstrated unequivocally by Miller *et al.* by tying together the donor and acceptor via a chemical linkage or bridge [24].

Because of its simplicity, Marcus theory has been used successfully to analyze a wide range of physical problems and is accepted as the "go-to" theory when describing charge and energy transfer in the condensed phase. However, there is a wealth of important dynamical information tucked away within this expression.

A number of years ago, our group developed a time-convolutionless master equation approach for computing state-to-state rates in which the coupling between states depends on the nuclear coordinates [25]. This approach incorporates a fully quantum-mechanical treatment of both the nuclear and electronic degrees of freedom and recovers the well-known Marcus expression in the semiclassical limit. The model is parameterized by the vibrational normal mode frequencies, and the electronic energies and energy derivatives at a reference configuration. The approach has been used by our group to compute state-to-state transition rates in semiempirical models for organic semiconducting light-emitting diodes and photovoltaics [17, 26–28].

We recently made a significant breakthrough in using this approach by tying it to a fully ab initio quantum chemical approach for determining the diabatic states and electron–phonon coupling terms, allowing unprecedented accuracy and utility for computing state-to-state electronic transition rates. Our methodology consists of two distinct components. The first is the use of a diabatization scheme for determining donor and acceptor states in a molecular unit. The other is a projection scheme which enables us to analyze the contribution of vibrations in reactions. Similar decomposition schemes have been presented in Ref. [29–31] and the approach used here builds upon the method given in Ref. [32]. We recently benchmarked this approach against both the experimental rates and recent theoretical rates presented by Subotnik *et al.* [33–35] and successfully applied the approach to compute state-to-state transition rates in series of Pt bridged donor–acceptor systems recently studied by Weinstein's group [18, 19, 36]. We review here these latter results along with the details of our methods.

II. THEORETICAL APPROACH

We consider a generic model for n electronic states coupled linearly to a phonon bath. Taking the electronic ground state of the system as a reference and assuming that the electronic states are coupled linearly to a common set of modes, we arrive at a generic form for the Hamiltonian, here written for two coupled electronic states:

$$H = \begin{pmatrix} \epsilon_1 & 0 \\ 0 & \epsilon_2 \end{pmatrix} + \begin{pmatrix} \mathbf{g}_{11} \cdot \mathbf{q} & \mathbf{g}_{12} \cdot \mathbf{q} \\ \mathbf{g}_{21} \cdot \mathbf{q} & \mathbf{g}_{22} \cdot \mathbf{q} \end{pmatrix} + \mathbf{I} \left(\frac{|\mathbf{p}|^2}{2} + \frac{1}{2} \mathbf{q}^T \cdot \boldsymbol{\Omega} \cdot \mathbf{q} \right). \tag{4}$$

Here, the first term contains the electronic energies, ϵ_1 and ϵ_2 computed at a reference geometry – typically that of the donor or acceptor state. The second term represents the linearized coupling between the electronic and nuclear degrees of freedom given in terms of the mass-weighted normal coordinates $\mathbf{q}$. The diagonal terms give the adiabatic displacement forces between the reference geometry and the two states. If we choose one of the states as the reference state, then either $\mathbf{g}_{11}$ or $\mathbf{g}_{22}$ will vanish. The remaining two terms correspond to the harmonic motions of the nuclear normal modes, given here in mass-weighted normal coordinates. In the normal mode basis, the Hessian matrix, $\boldsymbol{\Omega}$, is diagonal with elements corresponding to the normal mode frequencies, ω_j^2.

We now separate Eq. (4) into diagonal and off-diagonal terms,

$$\hat{H} = \hat{H}_o + \hat{V} \tag{5}$$

and recast the phonon operators in terms of the boson operators $[a_i, a_j^\dagger] = \delta_{ij}$. We then perform a polaron (shift) transform [25, 37, 38],

$$\begin{aligned} U &= \mathrm{e}^{-\sum_{ni} \frac{g_{nni}}{\hbar\omega_i} |n\rangle\langle n| (a_i^\dagger - a_i)} \\ &= \sum_n |n\rangle\langle n| \mathrm{e}^{-\sum_i \frac{g_{nni}}{\hbar\omega_i} (a_i^\dagger - a_i)} \end{aligned} \tag{6}$$

under which the transformed Hamiltonian is written in terms of the diagonal elements

$$\tilde{H}_0 = U^{-1} H_0 U = \sum_n \tilde{\epsilon}_n |n\rangle\langle n| + \sum_i \hbar\omega_i a_i^\dagger a_i, \tag{7}$$

with the renormalized electronic energies,

$$\tilde{\epsilon}_n = \epsilon_n - \sum_i \frac{g_{nni}^2}{\hbar\omega_i}, \tag{8}$$

and off-diagonal terms,

$$\hat{V}_{nm} = \sum_i g_{nmi} \left(a_i^\dagger + a_i - \frac{2g_{nni}}{\hbar\omega_i} \right) \mathrm{e}^{\sum_j \frac{(g_{nnj} - g_{mmj})}{\hbar\omega_j} (a_j^\dagger - a_j)}. \tag{9}$$

In the transformed (or dressed) picture, the electronic transition from state $|n\rangle$ to $|m\rangle$ is accompanied by the excitations of all the normal modes.

At this point, it is useful to connect the various terms in the phonon-dressed Hamiltonian with specific physical parameters. First, the reorganization energy is given by

$$\lambda_{nm} = \sum_j \frac{(g_{nnj} - g_{mmj})^2}{\omega_j} = \sum_j \hbar\omega_j S_j \tag{10}$$

where $\{S_j\}$ are the Huang-Rhys factors for each phonon mode. These are related to the Franck–Condon factor describing the overlap between the $v_j = 1$ vibronic state in one electronic state and the $v_j = 0$ vibronic state in the other. Likewise, the energy difference between the renormalized energy gaps is related to the driving force of the state-to-state transition,

$$\Delta E_{nm} = \tilde{\epsilon}_n - \tilde{\epsilon}_m. \tag{11}$$

Transforming to the interaction representation and performing a trace over the phonons give the spectral density in terms of the autocorrelation of the electron–phonon coupling operators. Using the explicit form of the electron–phonon coupling operators, one can arrive at a compact expression for the autocorrelation function of the electron–phonon coupling

$$\begin{aligned} C_{nm}(t) &= \langle V_{nm} V_{mn}(\tau) \rangle \qquad (12) \\ &= \sum_{i,j} g_{nmi} g_{mnj} ((\Delta_{nmi}(\bar{n}_i + 1)e^{i\omega_i\tau} - \Delta_{nmi}\bar{n}_i e^{-i\omega_i\tau} + \Omega_{nmi}) \\ &\quad \times (\Delta_{nmj}(\bar{n}_j + 1)e^{i\omega_j\tau} - \Delta_{nmj}\bar{n}_j e^{-i\omega_j\tau} + \Omega_{nmj}) \\ &\quad + \delta_{ij}(\bar{n}_i + 1)e^{i\omega_i\tau} + \delta_{ij}\bar{n}_i e^{-i\omega_i\tau}) q_{nm}(\tau) f_{nm}(\tau), \qquad (13) \end{aligned}$$

Here, $\hat{V}_{nm}(t)$ is the electron–phonon coupling term in the Heisenberg representation and $\langle \cdots \rangle$ denotes a thermal average over the vibrational degrees of freedom. The remaining terms are constructed from the normal mode frequencies $\{\omega_i\}$ and electron/nuclear couplings $\{g_{nmi}\}$ viz.

$$\Delta_{nmi} = \frac{(g_{nni} - g_{mmi})}{\omega_i}, \tag{14}$$

$$\Omega_{nmi} = \frac{(g_{nni} + g_{mmi})}{\omega_i}, \tag{15}$$

$$q_{nm}(\tau) = e^{i\sum_j \Delta^2_{nmj} \sin \omega_j \tau}, \tag{16}$$

$$f_{nm}(\tau) = e^{-2\sum_j (\bar{n}_j + \frac{1}{2})\Delta^2_{nmj}(1-\cos \omega_j \tau)}. \tag{17}$$

Finally, $\bar{n}_i$ is the Bose population of vibrational normal mode i,

$$\bar{n}_i = \frac{1}{e^{\beta\omega_i} - 1}. \tag{18}$$

The spectral density and golden-rule rate can then be obtained by Fourier transform

$$S_{nm}(\tilde{\omega}) = \int_{-\infty}^{\infty} \mathrm{d}t e^{-i\tilde{\omega}t} \langle \hat{V}_{nm}(t)\hat{V}_{mn}(0)\rangle. \tag{19}$$

and

$$k_{nm} = 2\mathrm{Re} \int_0^{\infty} \mathrm{d}t \left\langle \hat{V}_{nm}(0)\hat{V}_{mn}(t) \right\rangle e^{-i\tilde{\omega}_{nm}t}. \tag{20}$$

A. Semiclassical Rate Expression

To arrive at a Marcus-like expression for the rate constant, it is convenient to rewrite the diagonal and off-diagonal terms in terms of mass-scaled coordinates

$$H_o = \sum_n \epsilon_n |n\rangle\langle n| + \sum_{ni} \tilde{g}_{nni} |n\rangle\langle n| q_i + \sum_i \frac{p_i^2}{2} + \sum_i \frac{\omega_i^2 q_i^2}{2}, \tag{21}$$

and an off-diagonal part V

$$V = {\sum_{nmi}}' \tilde{g}_{nmi} |n\rangle\langle m| q_i, \tag{22}$$

where the electron–phonon coupling is given as

$$\tilde{g}_{nmi} = \sqrt{2\omega_i} g_{nmi}. \tag{23}$$

We now treat the coordinate and momentum operators as classical variables and obtain the golden-rule rate constants for the transition from state

$|n\rangle \to |m\rangle$ by averaging the golden-rule transition rates over the initial equilibrium distribution of the coordinates corresponding to the equilibrium ensemble for Hamiltonian H_o assuming that the initial electronic state of the system is $|n\rangle$

$$k_{nm} = 2\pi \int d\{q_i\} f(\{q_i\}) |V_{nm}(\{q_i\})|^2 \delta(U_n(\{q_i\}) - U_m(\{q_i\})), \quad (24)$$

where $\{q_i\}$ denotes all coordinate variables and

$$f(\{q_i\}) = \frac{1}{Z} e^{-\beta U_n(\{q_i\})} \quad (25)$$

and

$$V_{nm}(\{q_i\}) = \sum_i \tilde{g}_{nmi} q_i. \quad (26)$$

Here, Z is the partition function and $U_n(\{q_i\})$ is the total (diabatic) energy at nuclear configuration $\{q_i\}$

$$U_n(\{q_i\}) = \epsilon_n + \sum_i \tilde{g}_{nni} q_i + \sum_i \frac{\omega_i^2 q_i^2}{2}. \quad (27)$$

Note that Eq. (24) differs from the usual expressions by the presence of coordinate dependence in both the diagonal and off-diagonal coupling terms, $V_{nm}(\{q_i\})$. The integrations in Eq. (24) can be explicitly performed giving[1]

$$k_{nm} = |\tilde{H}_{nm}|^2 \sqrt{\frac{\pi}{k_B T \lambda_{nm}}} \exp\left(-\frac{(\Delta E_{nm} - \lambda_{nm})^2}{4 k_B T \lambda_{nm}}\right). \quad (28)$$

Here, the driving force and reorganization energy (between states n and m) are given by ΔE_{nm} and λ_{nm}

$$\Delta E_{nm} = \epsilon_n - \epsilon_m + \sum_i \frac{\tilde{g}_{mmi}^2 - \tilde{g}_{nni}^2}{2\omega_i^2}, \quad (29)$$

$$\lambda_{nm} = \sum_i \frac{(\tilde{g}_{nni} - \tilde{g}_{mmi})^2}{2\omega_i^2}. \quad (30)$$

Eq. (28) is similar to the Marcus expression in terms of relating the driving force and reorganization energy to the activation energy; however, the crucial difference is that the electronic matrix element is now temperature

---

[1] Note that Eq. (28) provides a correction to the original expression given in Ref. [25]. In our original paper, G_{nm} should have read P_{nm}.

dependent due to being renormalized by the phonons,

$$|\tilde{H}_{nm}|^2 = \left(\left(\frac{\Delta E_{nm} P_{nm}}{\lambda_{nm}} + F_{nm} \right)^2 + k_B T \left(H_{nm} - \frac{2P_{nm}^2}{\lambda_{nm}} \right) \right). \tag{31}$$

With P_{nm}, F_{nm}, and H_{nm} given by

$$P_{nm} = \sum_i \frac{\tilde{g}_{nmi}(\tilde{g}_{nni} - \tilde{g}_{mmi})}{2\omega_i^2}, \tag{32}$$

$$F_{nm} = \sum_i \frac{\tilde{g}_{nmi}(\tilde{g}_{nni} + \tilde{g}_{mmi})}{2\omega_i^2}, \tag{33}$$

$$H_{nm} = \sum_i \frac{\tilde{g}_{nmi}^2}{\omega_i^2}. \tag{34}$$

The latter of these is the unrenormalized electronic coupling. Lastly, it is easily verified from Eqs (24) or (28) that the forward and reverse rates satisfy detailed balance in that

$$\frac{k_{nm}}{k_{mn}} = e^{\beta \Delta E_{nm}}. \tag{35}$$

B. Parameterization from Ab Initio Quantum Chemistry

The formalism presented above requires both diagonal ($\mathbf{g}_{nn}$) and off-diagonal ($\mathbf{g}_{nm}$) derivative couplings between adiabatic states. However, accurate nonadiabatic couplings are difficult at best to obtain for even small molecules using state-of-the-art quantum chemical methods. A workaround is to transform to a diabatic representation, whereby the Hamiltonian is written as

$$\begin{aligned} H_{\text{dia}} &= U^T H_{\text{adia}} U \\ &= \begin{pmatrix} \epsilon_a(\mathbf{R}) + \mathrm{T}_{\mathrm{n}}'(\mathbf{R})_{11} & V_{ab} \\ V_{ab} & \epsilon_b(\mathbf{R}) + \mathrm{T}_n'(\mathbf{R})_{22} \end{pmatrix}. \end{aligned} \tag{36}$$

Figure 2 shows a sketch of the adiabatic and diabatic potentials for a model two-level system. While the adiabatic representation is precisely defined in terms of electronic eigenstates, the diabatic representation offers several advantages. First, the sharp derivative couplings that depend on the nuclear velocity in the adiabatic representation are transformed to smoother diabatic couplings, V_{ab}, that depend only on the nuclear positions. Second, the potential energy surfaces are smoother and the avoided crossing is eliminated. A number of diabatization approaches

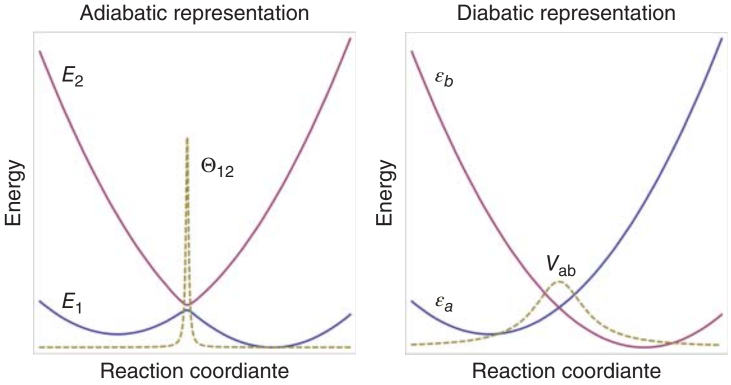

Figure 2. Sketch of adiabatic and diabatic representations for a two-state system. Compared to adiabatic representations, the diabatic representation has smoother energy surfaces and couplings. Reprinted (adapted) with permission from Yang and Bittner [39]. Copyright (2014) American Chemical Society.

have been developed and the reader is referred to Ref. [40] for a general review.

The problem now is how to obtain the transformation matrix

$$U = \begin{pmatrix} \cos\theta & \sin\theta \\ -\sin\theta & \cos\theta \end{pmatrix}. \tag{37}$$

While a number of methods are available [40], A straightforward approach is to eliminate derivative coupling mathematically by requiring

$$\langle \phi_i(\mathbf{r};\mathbf{R}) | \nabla_{\mathbf{R}} | \phi_j(\mathbf{r};\mathbf{R}) \rangle = 0. \tag{38}$$

However, this is computationally very expensive – especially for complex molecular systems, and exact solutions generally do not [41].

An alternative approach is to use physical intuition rather than a purely mathematical constraint to define the diabatic states. The Edmiston–Ruedenberg (ER) diabatization method is based on the idea that the diabatic states can be obtained by maximizing the total electron repulsion between localized states,

$$f_{\mathrm{ER}} = \sum_{k}^{N_{\text{states}}} dr_1 dr_2 \frac{\langle \phi_k | \hat{\rho}\,(r_1)\,| \phi_k \rangle \,\langle \phi_k | \hat{\rho}\,(r_2)\,| \phi_k \rangle}{\| r_1 - r_2 \|}. \tag{39}$$

When the adiabatic (and diabatic) energy minima are far enough away from the crossing points and the mixing angles between the diabatic and adiabatic states is small, we can use the gradients of the adiabatic potentials to approximate the diabatic potentials. Thus, if we perform calculations at the optimized geometry of the final acceptor state that is about Q_2 in Fig. 1), we can write the Hamiltonian as

$$H_{\text{dia},e} = \begin{pmatrix} \epsilon_1 & V_{12} \\ V_{21} & \epsilon_2 \end{pmatrix} + \begin{pmatrix} 0 & 0 \\ 0 & 1 \end{pmatrix} \mathbf{g}_{22} \cdot \mathbf{q} + H_{\text{osc}}, \tag{40}$$

where H_{osc} is the harmonic oscillator Hamiltonian for the vibrational normal modes. The linear assumption amounts to performing a series expansion of the full, multidimensional coupling term and keeping only the lowest order terms. Systematic improvement can be made by including higher-order (e.g., quadratic) off-diagonal couplings. However, this would involve a substantial increase in the complexity of the theory. The linear assumption is reasonable so long as the mixing angle is small [39, 42].

We obtain the diabatic couplings V_{12} and the mixing angle θ via ER localization and transform the electronic Hamiltonian from the adiabatic basis to the diabatic basis *viz.*

$$H_{\text{dia}} = \begin{pmatrix} \cos\theta & -\sin\theta \\ \sin\theta & \cos\theta \end{pmatrix} \begin{pmatrix} \epsilon_1 & 0 \\ 0 & \epsilon_2 \end{pmatrix} \begin{pmatrix} \cos\theta & \sin\theta \\ -\sin\theta & \cos\theta \end{pmatrix}. \tag{41}$$

The diabatic coupling is then given by

$$V_{ab} = \frac{1}{2}\sin 2\theta(\epsilon_2 - \epsilon_1). \tag{42}$$

We then diagonalize the electronic part and transform the electron/nuclear coupling back into the adiabatic basis. In doing so, we obtain the Hamiltonian in the form given in Eq. (4)

$$\begin{aligned} H &= U^T H_{\text{dia}} U \\ &= \begin{pmatrix} E_1 & 0 \\ 0 & E_2 \end{pmatrix} + \begin{pmatrix} \sin^2\theta & \frac{1}{2}\sin 2\theta \\ \frac{1}{2}\sin 2\theta & \cos^2\theta \end{pmatrix} \mathbf{g}_{22}.\mathbf{q} \\ &\quad + H_{\text{osc}}. \end{aligned} \tag{43}$$

Alternatively, one can use the generalized Mulliken–Hush model (GMH) [43, 44], which works well for linear systems, but does not generalize easily to systems with more than two charge centers. Within GMH, the diabatic mixing is given by

$$V_{12} = \frac{(E_2 - E_1)|\mu_{12}|}{\sqrt{(\mu_1 - \mu_2)^2 + 4\mu_{12}^2}},$$

where $(E_2 - E_1)$ is the vertical excitation energy, μ_1 and μ_2 are the dipole moments of the corresponding adiabatic states, and μ_{12} is the transition dipole moment between two states. ER localization can be seen as an extension of GMH that overcomes some drawbacks of GMH [34]. Both ER and GMH require convergence of the initial and final reference states and have be used to compute the coupling terms required for the TCLME approach given above [36, 39, 42].

C. Determining the Optimal Electron–Phonon Coupling Components

While the Marcus expression is elegant in its simplicity in requiring three parameters that can be obtained experimentally, it masks a wealth of details that underlie the quantum transition. Considerable insight into the state-to-state dynamics can be revealed by examining the nuclear motions driving and coupling the electronic states. Our approach is based on earlier work by our group [32] and Burghardt *et al.* [29–31]. Central to the theory is that there exists a collective nuclear displacement coordinate that connects the initial geometry of the donor to the final geometry of the acceptor. However, until this work, a general systematic approach for determining such motions did not exist.

Generally speaking, this collective coordinate involves all nuclear degrees of freedom. However, the form of the electronic Hamiltonian in Eq. (4) suggests that there exists a subset of motions that are specific modes that capture the majority of the electronic/nuclear coupling and give a dominant contribution to the collective reaction coordinate. Within the linearized approximation for the electronic/nuclear coupling, we can write a force tensor

$$\mathbf{F} = \begin{pmatrix} \mathbf{g}_{11} & \mathbf{g}_{12} \\ \mathbf{g}_{21} & \mathbf{g}_{22} \end{pmatrix} \tag{44}$$

where $\mathbf{F} \cdot \mathbf{q}$ is the electronic/nuclear coupling term in Eq. (4). If we consider each unique element $\{\mathbf{g}_{11}, \mathbf{g}_{12}, \mathbf{g}_{22}\}$ to be linearly independent, but nonorthogonal force vectors, one can develop a projection operator scheme to parse the N-dimensional linear vector space spanned by the mass-weighted normal mode vectors into two subspaces: one spanned by three vectors describing the coupling between the electronic states and the other spanned by the remaining $N - 3$ dimensional space spanned by motions that do not couple the electronic states. This subspace can be generated by defining a projection operator

$$\mathbf{P} = \sum_{\alpha\beta}{}' (\mathbf{S}^{-1})_{\alpha\beta} \mathbf{g}_\alpha \otimes \mathbf{g}_\beta \tag{45}$$

in which the summation is limited to linearly independent vectors. Here $\mathbf{S}_{\alpha\beta} = \mathbf{g}_\alpha \cdot \mathbf{g}_\beta$, Here $\otimes$ denotes the outer product, and $\mathbf{I}$ is the unit operator. This $N \times N$ matrix projects out all normal modes that are directly coupled to the electronic degrees of freedom and its complement $\mathbf{Q} = \mathbf{I} - \mathbf{P}$ projects out all modes not directly coupled. By diagonalizing the matrix

$$\mathbf{K} = \mathbf{P} \cdot \boldsymbol{\Omega} \cdot \mathbf{P} + \mathbf{Q} \cdot \boldsymbol{\Omega} \cdot \mathbf{Q} \tag{46}$$

we obtain a transformation, $\mathbf{M}$, between the normal coordinates and a new set of orthogonal coordinates. Both $\mathbf{P} \cdot \boldsymbol{\Omega} \cdot \mathbf{P}$ and $\mathbf{Q} \cdot \boldsymbol{\Omega} \cdot \mathbf{Q}$ are $N \times N$ matrices. However, for a two-state system, the former will have exactly 3 nontrivial eigenvalues, $\{\alpha_p\}$, with corresponding eigenvectors, $\{M_p\}$, whereas the latter will have exactly $N_r = N - 3$ nontrivial eigenvalues, $\{\alpha_q\}$, and corresponding eigenvectors, $\{M_q\}$. The full $N \times N$ transformation is formed by joining the nontrivial vectors from the two respective subspaces $\mathbf{M} = \{M_p, M_q\}$. The transformed electron–phonon coupling constants are given by projecting the couplings in the normal mode basis onto the new basis.

$$\mathbf{g}'_{ab} = \mathbf{M}_p \cdot \mathbf{g}_{ab}. \tag{47}$$

By examining the types of molecular motions that compose the $\mathbf{M}_p$ subspace, we can gain a deeper understanding of the specific classes of internal motion, which are directly involved with the ET process. In addition, we can gain a computational advantage since presumably this reduced set of modes gives the dominant contribution to the electron–phonon coupling and autocorrelation function given as the kernel in Eq. (20).

It is crucial to notice that the vectors given in Eq. (43) are *not linearly independent*. Consequently, special care must be taken to generate the reduced subspace. To facilitate this, we develop an iterative Lanczos approach, taking the normalized vector $\mathbf{v}_1 = \mathbf{g}_{22}$ as a starting point. As above, we initialize each step indexed by k, by defining a projection operator

$$\mathbf{P}_k = \mathbf{v}_k \otimes \mathbf{v}_k \tag{48}$$

and its complement $\mathbf{Q}_k = \mathbf{I} - \mathbf{P}_k$. for the kth mode. We also construct

$$\mathbf{P}_{\text{tot}} = \sum_k \mathbf{P}_k \tag{49}$$

as the total projection operator for all $k \leq N$ modes. We then project the Hessian matrix $\mathbf{\Omega}$ into each subspace *viz.*

$$\mathbf{\Omega}_p = \mathbf{P}_k \cdot \mathbf{\Omega} \cdot \mathbf{P}_k \ \& \ \mathbf{\Omega}_q = \mathbf{Q}_k \cdot \mathbf{\Omega} \cdot \mathbf{Q}_k \tag{50}$$

and diagonalize each to obtain eigenvalues and eigenvectors $\{\alpha_p, \mathbf{M}_p\}$ and $\{\alpha_q, \mathbf{M}_q\}$, respectively. As above, $\mathbf{\Omega}_p$ and $\mathbf{\Omega}_q$ are $N \times N$ matrices. The first set will have a single nontrivial eigenvalue and the second set will have $N - k$ nontrivial eigenvalues. As above, we collect the nontrivial eigenvectors associated with each to form the orthogonal transformation matrix

$$\mathbf{M}_k = \{\mathbf{M}_p, \mathbf{M}_q\}, \tag{51}$$

and again transform the full Hessian $\mathbf{\Omega}$ into this new vector space to form the $N \times N$ matrix $\mathbf{\Omega}'$. At each step in the iteration, the transformed Hessian, $\mathbf{\Omega}'$, is in the form of a $k \times k$ tridiagonal submatrix in the upper-left part of the matrix and a diagonal submatrix in the lower-right. For example, after $k = 3$ iterations, the Hessian matrix takes the form:

$$\mathbf{\Omega}' = \begin{pmatrix} \alpha_1 & b_1 & 0 & & & & 0 \\ b_1 & \alpha_2 & b_2 & & & & \\ 0 & b_2 & \alpha_3 & c_{k+1} & c_{k+2} & \cdots & c_N \\ & & c_{k+1} & \alpha_{k+1} & & & 0 \\ & & c_{k+2} & & \alpha_{k+2} & & \\ & & \vdots & & & \ddots & \\ 0 & & c_N & 0 & & & \alpha_N \end{pmatrix}. \tag{52}$$

We note that only the kth mode is coupled to the $N - k$ remaining modes. Since all of the transformations are orthogonal, diagonalizing $\mathbf{\Omega}'$ at any point returns the original Hessian matrix.

To continue iterating, we take the kth row of $\mathbf{\Omega}'$ and zero the first k elements

$$\mathbf{e} = \{0, \ldots 0, c_{k+1}, c_{k+2}, \ldots, c_N\}.$$

This is the coupling between the upper tridiagonal block and the lower diagonal block. We thus obtain a new vector

$$\mathbf{v}_{k+1} = \mathbf{e} \cdot \mathbf{M}$$

which is then reintroduced into the iteration scheme.

For the first iteration, $\mathbf{v}_1$ is parallel to the bare electron–phonon coupling vector g_{22} and the associated frequency is $\mathbf{v}_1 \cdot \Omega \cdot \mathbf{v}_1$. The subsequent iterations introduce corrections to this via phonon–phonon coupling mediated via the electronic couplings. For example, for the $k = 3$ iteration, we would determine the active vector space in terms of the upper-left 3×3 block of the matrix in Eq. (52).

$$\mathbf{\Omega}'_3 = \begin{pmatrix} \alpha_1 & b_1 & 0 \\ b_1 & \alpha_2 & b_2 \\ 0 & b_2 & \alpha_3 \end{pmatrix} \tag{53}$$

Diagonalizing $\mathbf{\Omega}'_3$ returns a set of frequencies and associated eigenvectors that are then used to compute the electron–phonon couplings in this reduced active space. After $N - 1$ iterations, $\mathbf{\Omega}'$ is a fully tridiagonal matrix and diagonalizing this returns the original normal mode basis.

At any point along the way, we can terminate the iteration and obtain a reduced set of couplings. Since the Lanczos approach uses the power method for finding the largest eigenvector of a matrix, it converges first upon the vector with the largest electron/nuclear coupling – which we refer to as the "primary mode." Subsequent iterations produce reduced modes with progressively weaker electron/nuclear couplings and the entire process can be terminated after a few iterations. After k-steps, the final electron–phonon couplings are then obtained by projecting the original set of couplings (in the normal mode basis) into the final vector space. For small systems, we find that accurate rates can be obtained with as few as two or three modes and that in many cases over 90% of the contribution to the rate comes from the first or "primary" mode identified by the projection approach [39, 42].

The method described above falls into the general class of "Mori chain" approximations, which provide hierarchical approximations to the memory kernel in Langevin dynamics [45, 46]. Furthermore, the approach belongs to the general class of power iteration methods that include the PageRank algorithm used by Google [47] and the "WTF" method used by Twitter to give users' recommendations of who to follow [48].

III. INELASTIC ELECTRONIC COUPLING IN DONOR–BRIDGE–ACCEPTOR COMPLEXES

The Weinstein group at the University of Sheffield reported recently upon a series of donor–bridge–acceptor (DBA) molecular triads whose ET pathways can be radically changed – even completely closed – by infrared light excitation of specific intramolecular vibrations [18, 19, 49]. The triads consist of a phenothiazine-based (PTZ) donor linked to a naphthalene monoimide (NAP) acceptor via a Pt-acetylide bridging unit [49]. The

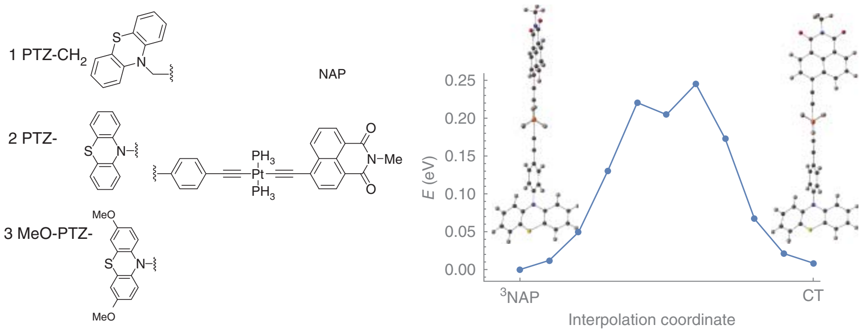

Figure 3. (a) Chemical structures of the donor (P), bridge (–Pt–), and acceptor (NAP) complexes considered here. (b) Triplet energy along a linear interpolation coordinate connecting the ^{3}NAP minimum energy geometry and the CT minimum energy geometry. Adapted from Yang *et al.* [36]. (*See color plate section for the color representation of this figure.*)

structures of the triads are given in Fig. 3(a). All three systems undergo a similar sequence of electron transfer processes following UV excitation: electron transfer from the Pt-acetylide center to the NAP acceptor, resulting in a charge-transfer state, $D - B^+ - A^-$, which due to strong spin–orbit coupling efficiently populates triplet charge-transfer state, CT. Further electron transfer leads to a fully charge-separated state (CSS) $D^+ - B - A^-$ with the electron and hole localized on the acceptor and donor units, respectively. The charge-transfer state can also undergo charge recombination to form a localized triplet exciton on the NAP unit (^{3}NAP), or the ground state. Both CSS and ^{3}NAP decay to the singlet ground state on the nanoseconds and submillisecond time scales, respectively. We also show in Fig. 3(b) the triplet energy along a linear interpolation coordinate connecting the ^{3}NAP minimum energy geometry to the CT minimum energy geometry. Between the two is a significant energy barrier reflecting the relative rotation of the NAP and the PTZ groups about the CC–Pt–CC axis.

The UV pump-IR push experiments performed on these triads showed that IR-excitation of bridge vibrations after the initial UV pump radically changes the relative yields of the intermediate states. Subsequent excitation of the –CC–Pt–CC– localized vibrations by a timed IR pulse in the CT state of the PTZ-complex **2** at 1 ps after the UV pump decreases the yield of the CSS state, whilst increasing that of the ^{3}NAP state. IR-excitation in the course of electron transfer has caused a 100% decrease in the CSS yield in **1**, approximately 50% effect in **2**, and no effect in **3**.

This demonstration of control over excited state dynamics strongly suggests that the acetylide stretching modes are significantly involved in the electron/nuclear coupling in these systems and play central roles in the electron-transfer process. The transferred charge can undergo either further separation to form the full CSS, or recombine to form a localized excitation, ^{3}NAP. Both eventually decay to ground state. Weinstein *et al.* showed that if a judiciously chosen IR pump is applied to excite the C≡C bond after the initial UV excitation, the yield of intermediate states can be radically changed. For example, when an IR pump with frequency = 1940 cm^{-1} is applied to excite the C≡C in PTZ-CH$_2$-Pt-NAP, 1 ps after the UV pump, the yield of the electron transfer state decreases from 32% to 15%, while that of the ^{3}NAP increases from 29% to 46%. The most striking observation is that when a 1908 cm^{-1} IR pulse is applied to PTZ-CH$_2$-Pt-NAP 2 ps after UV excitation, the CT → CSS step is completely switched off [18, 19, 49].

Quantum chemical analysis indicates that the electron-transfer rate is largely influenced by chemical modification of the PTZ donor. From PTZ-CH$_2$-Pt-NAP to PTZ-Pt-NAP, to OMe-PTZ-Pt-NAP, the donor strength increases, which increases the energy gap between CT and CSS states. The driving force (ΔG) for the CT → CSS transfer also increases from 0.2 eV in PTZ-CH$_2$-Pt-NAP, to 0.4 eV in PTZ-Pt-NAP, to 0.6 eV in OMe-PTZ-Pt-NAP. Large ΔG accelerates the CT decay and hence decreases the lifetime of the CT state. Comparing PTZ-Pt-NAP and PTZ-CH$_2$-Pt-NAP, CT transfer to both charge separation and recombination slows down by a factor of about 5 (the lifetime of CT increases from 3.3 to 14 ps and CSS from 190 ps to 1 ns). By appending methoxy groups to the PTZ, the donor strength is increased, and the reaction is accelerated. As a result, the lifetime of CT in OMe-PTZ-Pt-NAP is further reduced to 1 ps. Weinstein *et al.* proposed that the effect of infrared control is caused by the fact that the distance between CT energy minimum and the intersection of CT and CSS potential energy surfaces is small. For all three molecules, two PESs intersect where the C≡C bond is slightly longer than the equilibrium length. When the C≡C bond gets excited, it elongates and helps molecules to pass the intersection. If the energy gap between intersection and equilibrium geometry is much larger than C≡C vibrational energy, the dynamics is barely affected; if the energy gap is small, the vibrational excitation can radically change the dynamics [18, 19, 49].

A. Theoretical Model

We focus our attention on the PTZ system and anticipate that the other systems in this study will exhibit a similar behavior due to the overall similarity of the various donor groups [36]. For purposes of facilitating the calculations, the molecular structures are simplified such that the $P(Bu)_3$ moieties and octyl chain of the NAP group were truncated to $-PH_3$ and a single methyl group, respectively. In all quantum chemical calculations, we used the SDD pseudo-potential for Pt and 6-31G(d,p) for the other atoms. We also used the polarizable continuum model (PCM) to account for the dichloromethane solvent as used in Ref. [18, 19, 49]. The transition dipole moments and electron/hole distribution surfaces were calculated using the Multiwfn (v3.3.8) program [50]. An energy level diagram based on our calculations is sketched in Fig. 4(a) together with the corresponding electron/hole distribution plots.

To obtain the diabatic potentials and couplings, we perform a geometry optimization of both the lowest triplet (^{3}NAP) and the third triplet excited states (CT). As discussed below, we use the optimized states as reference geometries for determining the diabatic coupling within the GMH approximation [43, 44]. The normal modes and vibrational frequencies were obtained by harmonic expansion of the energy about the CT state. Once we have determined the diabatic states and couplings, we use the TCLME approach from Ref. [25] to compute the time-correlation functions and

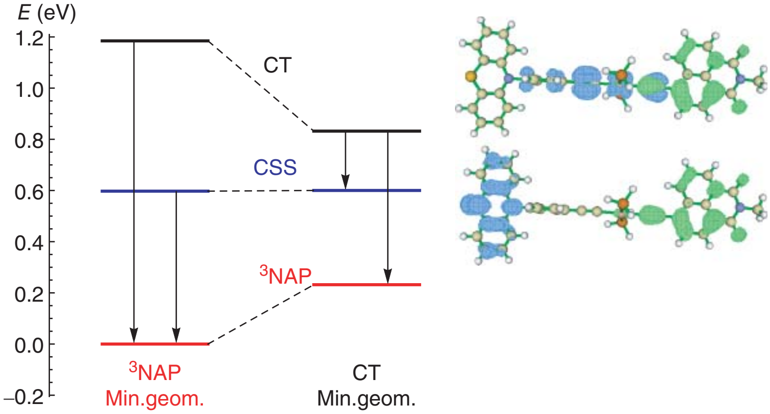

Figure 4. Energy level diagram for the triplet states of PTZ at the ^{3}NAP and CT state geometries. The electron/hole distributions for the CT and CSS are shown to the right (light gray = electron, dark gray = hole). Adapted from Yang *et al.* [36]. (*See color plate section for the color representation of this figure.*)

TABLE I

Comparison between Experimental and Computed State-to-State Transition Rates for PTZ

	CT geom.		^{3}NAP geom.	
Rates (ps^{-1})	CT→ CSS	CT→ ^{3}NAP	CT→ ^{3}NAP	CSS→ ^{3}NAP
Exp.	0.0879	0.097	0.097	1.84E−3
Marcus	0.846	0.2043	1002.82	8.250E−11
Marcus (mean V)	365.7	12.75	95.23	5.04E−6
TCLME	0.725	0.0562	12.89	3.022E−8
TCLME + PLM	0.627	0.0488	21.6	0.500E−4
TCLME (mean V)	–	2.79	8.931	1.51E−3

The experimental rates for each process are obtained from Ref. [19] and we assume a common temperature of 300K for the experiments and calculations.
Adapted from Yang *et al.* [36].

state-to-state golden-rule rates as discussed above. We also use the projection technique to determine an optimal set of normal modes and determine the number of such optimal modes that are required to converge the time-correlation functions to a desired degree of accuracy. We then use both the CT and ^{3}NAP minima as reference states for computing the diabatic potentials and couplings necessary for computing rates and modes. Those obtained at the CT minimum can be used to compute transitions originating in from the CT state, while those obtained at the ^{3}NAP minimum can be used for transitions terminating in the ^{3}NAP state.

We now compare ET rates as computed using both Marcus theory and the TCLME approach. Table I summarizes both the experimental and computed state-to-state rates for the PTZ system. For the TCLME approach, we examine the convergence of both the time-correlation functions and the rate constants with respect to the number of nuclear modes included in the summation in the construction of the electron–phonon coupling in Eq. (9). For our purposes, an "exact" calculation involves including all nuclear vibrational modes. In our previous work, we showed that both $C(t)$ and the total transfer rate constant, k_{nm}, calculated using only the first few projected modes provide an excellent agreement with the exact quantities computed using the full set of normal modes, as well as the experimental rates, when parameterized using accurate quantum chemical data [39, 42].

B. Marcus Theory Rates

The Marcus expression provides a succinct means for computing transition rates from the driving force ΔG°, diabatic coupling V_{ab} and reorganization

TABLE II

Driving force ΔG°, reorganization energy λ, diabatic coupling V, mean diabatic coupling $\bar{V}$, and $\Delta G^\circ_{\bar{V}}$ (driving force calculated with $\bar{V}$), for different transitions

	^{3}NAP geom. (0 eV)		CT geom. (0.818 eV)	
	CSS→^{3}NAP	CT→^{3}NAP	CT→^{3}NAP	CT→CSS
ΔG° (eV)	0.414	−0.913	−0.781	−0.20
λ (eV)	1.01	0.271	1.38	1.08
V(eV)	2.56E−4	0.345	1.34E−2	9.22E−3
$\bar{V}$ (eV)	6.34E−2	0.106	0.106	0.192
$\Delta G^\circ_{\bar{V}}$ (eV)	0.414	−0.851	−0.770	N/A

Adapted with from Yang *et al.* [36].

energy λ in Eq. (1). In Table II, we provide a summary of the parameters computed for the transitions we are considering. The two columns under the heading labeled ^{3}NAP correspond to parameters computed using the ^{3}NAP minimum as a reference geometry while those under the heading labeled CT correspond to parameters computed using the CT reference geometry.

The Marcus rates provide a useful benchmark for our approach. Moreover, the parameters in this table portend a difficulty in using the ^{3}NAP geometry as a reference. For example, for the CSS → ^{3}NAP transition, the driving force is in the wrong direction since it predicts that the CSS state lies lower in energy than the ^{3}NAP state, which is inconsistent with both experimental observations and our quantum chemical analysis in Fig. 4.

C. TCLME Rates

To compute the rates using the TCLME expression (Eq. (20)), we begin by computing the electron/nuclear correlation function and compare its convergence with respect to the number of Lanczos modes. Recall that the Lanczos modes are determined by an iterative ranking algorithm that identifies superpositions of normal modes that optimize the electron–phonon coupling. The method is akin to the short-iterative Lanczos method developed by Park and Light for quantum dynamics [51].

Figure 5 gives a summary of these numerical tests in which we compute $C_{nm}(t)$ versus time with an increasing number of Lanczos modes. In all cases, we compare to the "exact" result in which all nuclear modes were used. The top two figures (Fig. 5a and b) use the ^{3}NAP as the reference geometry. In these cases, convergence of $C_{nm}(t)$ with respect

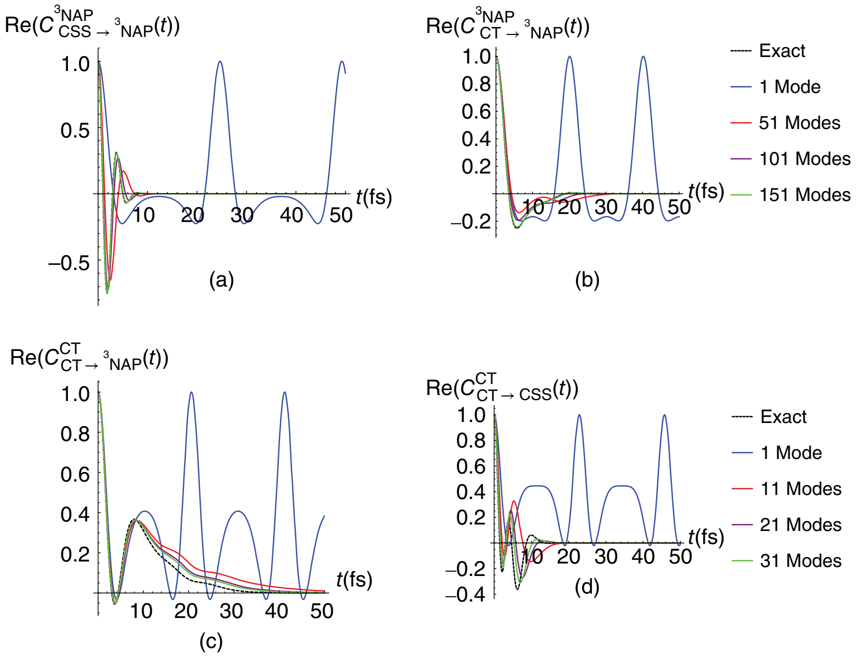

Figure 5. Correlation functions of various numbers of projected modes, compared to the exact correlation, for (a) CSS → ^{3}NAP at ^{3}NAP geometry, (b) CT → ^{3}NAP at ^{3}NAP geometry, (c) CT → ^{3}NAP at CT geometry, and (d) CT → CSS at CT geometry. Adapted with from Yang *et al.* [36]. (*See color plate section for the color representation of this figure.*)

to the number of modes proved to be problematic for both transitions considered. Correspondingly, the rates computed using this geometry also compare poorly against the observed experimental rates, although they are an order of magnitude closer than Marcus rates. We speculate that this may signal a breakdown in the Condon approximation, which ensures separability between nuclear and electronic degrees of freedom.

Given the complexity and size of the system, overall the numerical rates computed using the exact TCLME approach are in quantitative agreement with the experimental rates, particularly for those using the CT geometry as a reference point (cf. Fig. 5c and d). We note that fewer projected modes (30–50) are needed to converge the correlation function out to the first 50 fs when using the CT-geometry. Furthermore, while the Marcus rate for the CT → CSS transition agrees with the exact TCLME result, it misses the CT → ^{3}NAP experimental rate by four orders of magnitude whereas the TCLME rate is in much better agreement with the experimental rate.

If we compare the exact TCLME rate, which uses the full set of normal modes in constructing the $C_{nm}(t)$ correlation function, to the rate computed using *only* the PLM (TCLME + PLM), for both the CT → CSS and CT to ^{3}NAP rates, the single mode approximation is within 86% of the exact result. This indicates that while multiple vibrational normal modes contribute to the electronic coupling, the linear combination identified by the projection algorithm carries the vast majority of the electron–phonon coupling. This is consistent with our previous study of triplet energy transfer in small donor-bridge-acceptor systems [39, 42].

D. Primary Mode Approximation

As discussed earlier, our ranking algorithm allows us to rapidly determine the vibrational motions that optimize the electron/nuclear couplings. In addition to providing an accurate way to compute rate constants, they provide additional insight into actual dynamics. Here, we shall focus on the transitions originating from the CT geometry. Generally speaking, the highest ranked mode, termed the "primary Lanczos mode" (PLM), captures much of the short-time dynamics of the transitions. In Fig. 5, we show the electronic coupling correlation functions computed using different numbers of projected modes for all four transitions. For the CT → ^{3}NAP transition, the primary mode resembles the exact initial dynamics for the first 10 fs and roughly 10 or so modes are sufficient to converge the correlation function out to times longer than the correlation time. In Table I, we see that for the CT geometry, the primary mode approximation is sufficient to obtain accurate rate constants. On the contrary, it takes considerably more modes to recover the full correlation function for transition originating from the ^{3}NAP geometry.

Figure 6(a–d) shows the projection of the primary mode identified for each transition onto the normal vibrational modes of the originating state, that is, the primary modes calculated at CT geometry are projected onto the normal modes of the CT state, and those at the ^{3}NAP geometry are projected onto the normal modes of the ^{3}NAP state. In all four cases, the primary mode is dominated by symmetric and antisymmetric contributions from the C≡C displacements. While both transitions involve acetylene bond-stretching motions, the CT → CSS transition involves only the *symmetric* combination, whereas the CT → ^{3}NAP involves both the *symmetric* and *antiasymmetric* combination. It is tempting to conclude from this that the secondary IR push used in the experiments preferentially

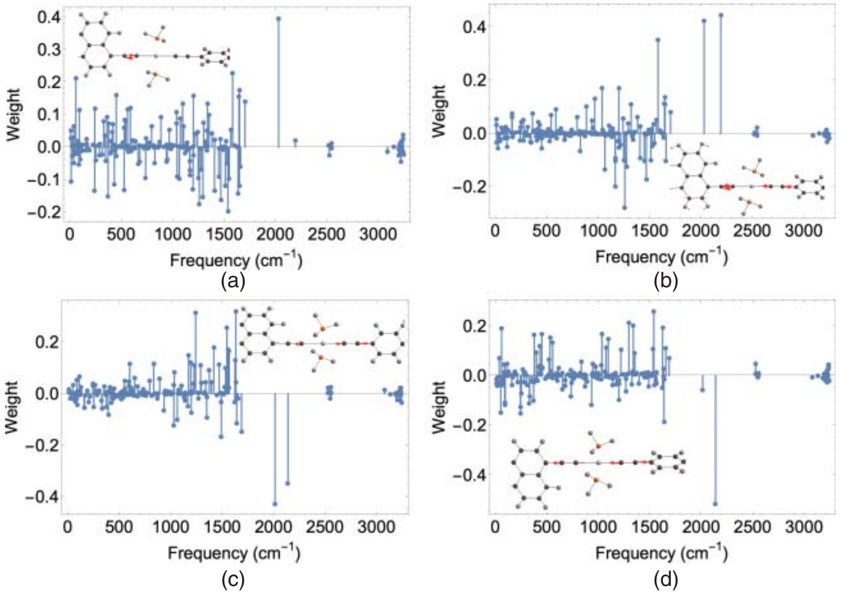

Figure 6. Component projection of the primary mode onto the normal modes for the following transitions: (a) CSS → ^{3}NAP, (b) CT → ^{3}NAP calculated at ^{3}NAP geometry. (c)CT → ^{3}NAP, and (d) CT → CSS calculated at CT geometry. The embedded molecule shows the atomic displacement vectors of primary mode. Adapted from Yang *et al.* [36]. (*See color plate section for the color representation of this figure*.)

excites the antisymmetric mode and thus selectively enhances the CT → ^{3}NAP transition. In fact, the computed IR oscillator strength of the antisymmetric mode is an order of magnitude greater than the symmetric mode. Similarly, from experiment, the antisymmetric normal mode extinction coefficient is three times larger than that for the symmetric normal mode. However, the time scale for the IR excitation is sufficiently long enough that *both* symmetric and antisymmetric CC modes are expected to be equally populated by the IR push pulse.

In the CT → ^{3}NAP transition, both types of acetylene stretching motions (symmetric and antisymmetric) contribute more or less equally to the electronic coupling while in the CT → CSS transition, *only* the symmetric acetylene motion carries the majority of the coupling. This mechanism can be rationalized by the way the vibrational populations enter into our expression for electron/nuclear coupling correlation function in Eq. (13). In principle, the expression was derived assuming a thermal population of the vibrational modes. However, if we assume that the role of the IR pulse is to excite the C≡C stretching modes by one vibrational quantum, then the value of $\bar{n}_i$ appearing in Eq. (13) for those modes should be increased to $\bar{n}_i + 1$. Consequently, driving these modes with the IR pulse *increases* the total electronic coupling, consistent with the experimental observation that IR excitation following formation of the CT states accelerates the CT → ^{3}NAP transition relative to the CT →CSS transition.

IV. DISCUSSION

We present here a review of our work in developing new tools for analyzing electronic transitions in complex molecular systems. Central to our work is the notion that one can systematically identify a subset of vibrational modes that capture the majority of the electronic coupling to the nuclear motions. These primary modes capture the short-time dynamics with sufficient accuracy for computing the salient correlation and response functions necessary for evaluating the golden-rule rates for state-to-state transitions. While not a central theme to this review, our time-convolutionless master equation method can be used for computing multistate transitions and in cases where the state-to-state rates are time-dependent [26, 32].

Our approach offers several distinct advantages over other methods. First, and certainly foremost, we use as input parameters molecule specific information derived directly from accurate ab initio quantum chemical methods. We also include in this the influence of the solvent and in principle can include coupling to multiple electronic states. Thus, the spectral density used in our approach should accurately reflect the spectral density of the true physical system. We believe that the key to understanding and ultimately controlling ET pathways in a complex molecular species is through vibronic coupling. The approach we have delineated in this article offers a systematic way to deduce a subset of nuclear motions that are most responsible for driving electronic transitions. When paired with the TCLME approach for computing the state-to-state transitions, we can obtain rate constants that are in quantitative agreement with experimental rates and probe deeper into the dynamics to understand which specific types of nuclear motions are involved in a given transition. The algorithm illustrated here in the example of photoinduced charge transfer should be of considerable utility for understanding of a multitude of light-induced reactions where several electronic states are involved in ultrafast transformations.

ACKNOWLEDGMENTS

XY thanks Tian Lu for help with Multiwfn. The work at the University of Houston was funded in part by the National Science Foundation (CHE-1362006, MRI-1531814) and the Robert A. Welch Foundation (E-1337). We thank the Weinstein group at the University of Sheffield for sharing their experimental results and many detailed conversations regarding the PTZ-Pt-NAP triad. Figures 3–5, and 6 and Tables I and II are reproduced from Yang *et al.* [36] and are licensed under the Creative Commons Attribution 4.0 International License. To view a copy of this license, visit http://creativecommons.org/licenses/by/4.0/

REFERENCES

1. Yoon, M.C., Jeong, D.H., Cho, S., Kim, D., Rhee, H., and Joo, T. (2003) Ultrafast transient dynamics of Zn(II) porphyrins: observation of vibrational coherence by controlling chirp of femtosecond pulses. *J. Chem. Phys.*, **118** (1), 164–171. doi: 10.1063/1.1524175.
2. Gruia, F., Ionascu, D., Kubo, M., Ye, X., Dawson, J., Osborne, R.L., Sligar, S.G., Denisov, I., Das, A., Poulos, T.L., Terner, J., and Champion, P.M. (2008) Low-frequency dynamics of caldariomyces fumago chloroperoxidase probed by femtosecond coherence spectroscopy. *Biochemistry*, **47** (18), 5156–5167. doi: 10.1021/bi7025485. pMID: 18407660.
3. Zhu, L., Sage, J., and Champion, P. (1994) Observation of coherent reaction dynamics in heme proteins. *Science*, **266** (5185), 629–632. doi: 10.1126/science.7939716.
4. Rosca, F., Kumar, A.T.N., Ionascu, D., Ye, X., Demidov, A.A., Sjodin, T., Wharton, D., Barrick, D., Sligar, S.G., Yonetani, T., and Champion, P.M. (2002) Investigations of anharmonic low-frequency oscillations in heme proteins. *J. Phys. Chem. A*, **106** (14), 3540–3552. doi: 10.1021/jp0129277.
5. Delfino, I., Manzoni, C., Sato, K., Dennison, C., Cerullo, G., and Cannistraro, S. (2006) Ultrafast pump-probe study of excited-state charge-transfer dynamics in umecyanin from horseradish root. *J. Phys. Chem. B*, **110** (34), 17252–17259. doi: 10.1021/jp062904y. pMID: 16928024.
6. Reid, P.J., Silva, C., Barbara, P.F., Karki, L., and Hupp, J.T. (1995) Electronic coherence, vibrational coherence, and solvent degrees of freedom in the femtosecond spectroscopy of mixed-valence metal dimers in H2O and D2O. *J. Phys. Chem.*, **99** (9), 2609–2616. doi: 10.1021/j100009a019.
7. Schwartz, B.J., Bittner, E.R., Prezhdo, O.V., and Rossky, P.J. (1996) Quantum decoherence and the isotope effect in condensed phase nonadiabatic molecular dynamics simulations. *J. Chem. Phys.*, **104** (15), 5942–5955. http://link.aip.org/link/?JCP/104/5942/1.
8. Schwartz, B.J. and Rossky, P.J. (1996) The isotope effect in solvation dynamics and nonadiabatic relaxation: a quantum simulation study of the photoexcited

solvated electron in d[sub 2]O. *J. Chem. Phys.*, **105** (16), 6997–7010. doi: 10.1063/1.471989.

9. Bittner, E.R. and Rossky, P.J. (1995) Quantum decoherence in mixed quantum-classical systems: nonadiabatic processes. *J. Chem. Phys.*, **103** (18), 8130–8143. http://link.aip.org/link/?JCP/103/8130/1.
10. Webster, F.J., Schnitker, J., Friedrichs, M.S., Friesner, R.A., and Rossky, P.J. (1991) Solvation dynamics of the hydrated electron: a nonadiabatic quantum simulation. *Phys. Rev. Lett.*, **66** (24), 3172–3175. doi: 10.1103/PhysRevLett.66.3172.
11. Auböck, G. and Chergui, M. (2015) Sub-50-fs photoinduced spin crossover in $Fe(bpy)_3^{2+}$. *Nat. Chem.*, **7** (8), 629–633. doi: 10.1038/nchem.2305.
12. Schrauben, J.N., Dillman, K.L., Beck, W.F., and McCusker, J.K. (2010) Vibrational coherence in the excited state dynamics of $Cr(acac)_3$: probing the reaction coordinate for ultrafast intersystem crossing. *Chem. Sci.*, **1**, 405–410. doi: 10.1039/C0SC00262C.
13. Rozzi, C.A., Falke, S.M., Spallanzani, N., Rubio, A., Molinari, E., Brida, D., Maiuri, M., Cerullo, G., Schramm, H., Christoffers, J., and Lienau, C. (2013) Quantum coherence controls the charge separation in a prototypical artificial light-harvesting system. *Nat. Commun.*, **4**, 1602. doi: 10.1038/ncomms2603.
14. Falke, S.M., Rozzi, C.A., Brida, D., Maiuri, M., Amato, M., Sommer, E., De Sio, A., Rubio, A., Cerullo, G., Molinari, E., and Lienau, C. (2014) Coherent ultrafast charge transfer in an organic photovoltaic blend. *Science*, **344** (6187), 1001–1005. doi: 10.1126/science.1249771.
15. Grancini, G., Maiuri, M., Fazzi, D., Petrozza, A., Egelhaaf, H.J., Brida, D., Cerullo, G., and Lanzani, G. (2013) Hot exciton dissociation in polymer solar cells. *Nat. Mater.*, **12** (1), 29–33. doi: 10.1038/nmat3502.
16. Jailaubekov, A.E., Willard, A.P., Tritsch, J.R., Chan, W.L., Sai, N., Gearba, R., Kaake, L.G., Williams, K.J., Leung, K., Rossky, P.J., and Zhu, X.Y. (2013) Hot charge-transfer excitons set the time limit for charge separation at donor/acceptor interfaces in organic photovoltaics. *Nat. Mater.*, **12** (1), 66–73. doi: 10.1038/nmat3500.
17. Bittner, E.R. and Silva, C. (2014) Noise-induced quantum coherence drives photo-carrier generation dynamics at polymeric semiconductor heterojunctions. *Nat. Commun.*, **5**, 3119. doi: 10.1038/ncomms4119.
18. Delor, M., Scattergood, P.A., Sazanovich, I.V., Parker, A.W., Greetham, G.M., Meijer, A.J., Towrie, M., and Weinstein, J.A. (2014) Toward control of electron transfer in donor-acceptor molecules by bond-specific infrared excitation. *Science*, **346** (6216), 1492–1495.
19. Delor, M., Keane, T., Scattergood, P.A., Sazanovich, I.V., Greetham, G.M., Towrie, M., Meijer, A.J., and Weinstein, J.A. (2015) On the mechanism of vibrational control of light-induced charge transfer in donor–bridge–acceptor assemblies. *Nat. Chem.*, **7**, 689–695. doi: 10.1038/nchem.2327.
20. Marcus, R.A. (1956) On the theory of oxidation-reduction reactions involving electron transfer. I. *J. Chem. Phys.*, **24** (5), 966–978.
21. Marcus, R.A. (1965) On the theory of electron-transfer reactions. VI. Unified treatment for homogeneous and electrode reactions. *J. Chem. Phys.*, **43** (2), 679–701.
22. Marcus, R.A. (1993) Electron transfer reactions in chemistry. Theory and experiment. *Rev. Mod. Phys.*, **65** (3), 599–610.

23. Rehm, D. and Weller, A. (1969) Kinetik und mechanismus der elektronenübertragung bei der fluoreszenzlöschung in acetonitril. *Ber. Bunsen Ges. Phys. Chem.*, **73**, 832–839.
24. Miller, J., Calcaterra, L., and Closs, G. (1984) Intramolecular long-distance electron transfer in radical anions. The effects of free energy and solvent on the reaction rates. *J. Am. Chem. Soc.*, **106** (10), 3047–3049.
25. Pereverzev, A. and Bittner, E.R. (2006) Time-convolutionless master equation for mesoscopic electron–phonon systems. *J. Chem. Phys.*, **125** (10), 104906.
26. Tamura, H., Ramon, J.G., Bittner, E.R., and Burghardt, I. (2008) Phonon-driven ultrafast exciton dissociation at donor-acceptor polymer heterojunctions. *Phys. Rev. Lett.*, **100** (10), 107402.
27. Tamura, H., Bittner, E.R., and Burghardt, I. (2007) Exciton dissociation at donor-acceptor polymer heterojunctions: quantum nonadiabatic dynamics and effective-mode analysis. *J. Chem. Phys.*, **126** (2), 021103.
28. Singh, J., Bittner, E.R., Beljonne, D., and Scholes, G.D. (2009) Fluorescence depolarization in poly[2-methoxy-5-((2-ethylhexyl)oxy)-1, 4-phenylenevinylene]: sites versus eigenstates hopping. *J. Chem. Phys.*, **131** (19), 194905.
29. Cederbaum, L.S., Gindensperger, E., and Burghardt, I. (2005) Short-time dynamics through conical intersections in macrosystems. *Phys. Rev. Lett.*, **94** (11), 113003.
30. Gindensperger, E., Burghardt, I., and Cederbaum, L.S. (2006) Short-time dynamics through conical intersections in macrosystems. I. Theory: effective-mode formulation. *J. Chem. Phys.*, **124** (14), 144103.
31. Gindensperger, E., Burghardt, I., and Cederbaum, L.S. (2006) Short-time dynamics through conical intersections in macrosystems. II. Applications. *J. Chem. Phys.*, **124** (14), 144104.
32. Pereverzev, A., Bittner, E.R., and Burghardt, I. (2009) Energy and charge-transfer dynamics using projected modes. *J. Chem. Phys.*, **131** (3), 034104.
33. Subotnik, J.E., Yeganeh, S., Cave, R.J., and Ratner, M.A. (2008) Constructing diabatic states from adiabatic states: extending generalized Mulliken–Hush to multiple charge centers with boys localization. *J. Chem. Phys.*, **129** (24), 244101.
34. Subotnik, J.E., Cave, R.J., Steele, R.P., and Shenvi, N. (2009) The initial and final states of electron and energy transfer processes: diabatization as motivated by system-solvent interactions. *J. Chem. Phys.*, **130** (23), 234102.
35. Subotnik, J.E., Vura-Weis, J., Sodt, A.J., and Ratner, M.A. (2010) Predicting accurate electronic excitation transfer rates via Marcus theory with Boys or Edmiston–Ruedenberg localized diabatization. *J. Phys. Chem. A*, **114** (33), 8665–8675.
36. Yang, X., Keane, T., Delor, M., Meijer, A.J.H.M., Weinstein, J., and Bittner, E.R. (2017) Identifying electron transfer coordinates in donor-bridge-acceptor systems using mode projection analysis. *Nat. Commun.*, **8**, 14554. doi: 10.1038/NCOMMS14554.
37. Grover, M.K. and Silbey, R. (1970) Exciton–phonon interactions in molecular crystals. *J. Chem. Phys.*, **52** (4), 2099–2108.
38. Rice, M. and Gartstein, Y.N. (1994) Excitons and interband excitations in conducting polymers based on phenylene. *Phys. Rev. Lett.*, **73** (18), 2504–2507.

39. Yang, X. and Bittner, E.R. (2014) Intramolecular charge- and energy-transfer rates with reduced modes: comparison to Marcus theory for donor–bridge–acceptor systems. *J. Phys. Chem. A*, **118** (28), 5196–5203.
40. Domcke, W., Yarkony, D.R., and Köppel, H. (2004) *Conical Intersections: Electronic structure, Dynamics and Spectroscopy*, Advanced Series in Physical Chemistry, vol. **15**, World Scientific Co.
41. Mead, C.A. and Truhlar, D.G. (1982) Conditions for the definition of a strictly diabatic electronic basis for molecular systems. *J. Chem. Phys.*, **77** (12), 6090–6098.
42. Yang, X. and Bittner, E.R. (2015) Computing intramolecular charge and energy transfer rates using optimal modes. *J. Chem. Phys.*, **142** (24), 244114.
43. Cave, R.J. and Newton, M.D. (1996) Generalization of the Mulliken-Hush treatment for the calculation of electron transfer matrix elements. *Chem. Phys. Lett.*, **249** (1), 15–19.
44. Cave, R.J. and Newton, M.D. (1997) Calculation of electronic coupling matrix elements for ground and excited state electron transfer reactions: comparison of the generalized Mulliken–Hush and block diagonalization methods. *J. Chem. Phys.*, **106** (22), 9213–9226.
45. Mori, H. (1965) Transport, collective motion, and Brownian motion. *Prog. Theor. Phys.*, **33** (3), 423–455. doi: 10.1143/PTP.33.423.
46. Vesely, F. (1984) Algorithms for Mori chain dynamics: a unified treatment. *Mol. Phys.*, **53** (2), 505–524. doi: 10.1080/00268978400102481.
47. Brin, S. and Page, L. (1998) The anatomy of a large-scale hypertextual web search engine. *Comput. Networks ISDN Syst.*, **30** (1), 107–117. doi: http://dx.doi.org/10.1016/S0169-7552(98)00110-X.
48. Gupta, P., Goel, A., Lin, J., Sharma, A., Wang, D., and Zadeh, R. (2013) WTF: the who to follow service at Twitter, in *Proceedings of the 22nd International Conference on World Wide Web, ACM, New York, NY, USA, WWW '13*, pp. 505–514. doi: 10.1145/2488388.2488433.
49. Scattergood, P.A., Delor, M., Sazanovich, I.V., Bouganov, O.V., Tikhomirov, S.A., Stasheuski, A.S., Parker, A.W., Greetham, G.M., Towrie, M., Davies, E.S. et al. (2014) Electron transfer dynamics and excited state branching in a charge-transfer platinum (II) donor–bridge-acceptor assembly. *Dalton Trans.*, **43** (47), 17677–17693.
50. Lu, T. and Chen, F. (2012) Multiwfn: a multifunctional wavefunction analyzer. *J. Comput. Chem.*, **33** (5), 580–592.
51. Park, T.J. and Light, J.C. (1986) Unitary quantum time evolution by iterative Lanczos reduction. *J. Chem. Phys.*, **85**, 5870–5876.